Research Article Vol. 2, No. 11 / 15 Nov 2023 / Optics Continuum 2333
OPTICS CONTINUUM

RedEye-1: a compact SWIR hyperspectral imager for observation of atmospheric methane and carbon dioxide

NAIF ALSALEM,[1,2,*] CHRISTOPHER H. BETTERS,[1,3,4] YIWEI MAO,[1] IVER H. CAIRNS,[1] AND SERGIO G. LEON-SAVAL[1,3,4]

[1]ARC Training Centre for CubeSats, UAVs and Their Applications (CUAVA), School of Physics, University of Sydney, Sydney, NSW 2006, Australia
[2]Ministry of Education, Riyadh, Saudi Arabia
[3]Sydney Institute for Astronomy (SIfA), University of Sydney, School of Physics, Sydney, NSW 2006, Australia
[4]Sydney Astrophotonic Instrumentation Laboratory (SAIL), School of Physics, University of Sydney, Sydney, NSW 2006, Australia
*naif.alsalem@sydney.edu.au

Abstract: We present the development of our first prototype of a compact short-wavelength infrared (SWIR) hyperspectral imager, RedEye-1, designed to observe and measure the concentrations of methane (CH_4) and carbon dioxide (CO_2) in the atmosphere. It operates in the spectral range of 1588 nm to 1673 nm with a nominal spectral resolution of 0.5 nm and has a total weight of approximately 1.8 kg. We outline the optical design of the instrument, including its fore-optics (telescope), and evaluate its performance using the OpticStudio ZEMAX software. In addition, we explain the spectral and radiometric calibration procedures and present the results. Our preliminary data reduction and analysis revealed a high quality SWIR image and a single path measurement of an atmospheric profile displaying the absorption lines of CH_4 and CO_2.

1. Introduction

Spectral remote sensing imagers, also known as hyperspectral or multispectral imagers, play a key role in a wide variety of applications ranging from environmental research to agriculture monitoring, search and rescue, and target detection and identification [1–4]. The development of high-resolution, compact imagers is challenging due to the high costs of custom-made optics, detectors, and manufacturing. The challenge can become a hurdle if the imager operates in the short-, middle-, and / or long-wavelength infrared (SWIR, MWIR, LWIR) parts of the spectrum, which require special optics and detectors. Moreover, SWIR, MWIR and LWIR detectors are often export controlled because of their dual-use nature. However, commercial-off-the-shelf (COTS) components, to some extent, play a key role in the rapid development of compact hyperspectral imagers for Earth observation applications from air- and space-borne platforms. For example, a do-it-yourself compact imager was developed using COTS and 3D printed parts to acquire hyperspectral images [5]. A more optimised version (HSI V6) operated in the spectral interval 400 – 800 nm with a spectral resolution close to 3.69 nm at 546.1 nm [6]. A new, optimised version of Ref. [5]'s hyperspectral imager with an open-source Python library (OpenHSI) was also developed with COTS components and 3D printed parts [7]. OpenHSI is a pushbroom instrument that collected hyperspectral images through a field-of-view (FOV) of 10.6° in the spectral range 400–830 nm with a 1.5 nm spectral resolution and an Instantaneous field of view (iFOV) of about 1.5 mrad.

The composition of the atmosphere of Earth is of continuing interest for both long- and short-term studies and analyses due to its critical role in the development and maintenance of life on Earth [8]. In particular, the chemical composition of Earth's atmosphere has attracted wide

#494570 https://doi.org/10.1364/OPTCON.494570
Journal © 2023 Received 2 May 2023; revised 19 Oct 2023; accepted 20 Oct 2023; published 2 Nov 2023

OPTICS CONTINUUM

attention from both the atmospheric and space physics communities, working to detect, measure and evaluate atmospheric molecules and suspended particles present as a function of position and time of day. Atmospheric molecules such as CO_2, CH_4, H_2O, CO, and N_2O are of particular interest due to their role in trapping heat in the atmospheric layers [9] leading to what is known as the greenhouse effect [10–12]. Many instruments were designed and developed to allow air- and space-based measurements of atmospheric gases. They can be categorised into two groups: (1) large instruments with high spectral resolution and (2) compact instruments with lower spectral resolution. Space missions such as Orbiting Carbon Observatory-2 (OCO-2) [13], Greenhouse Gases Observing Satellite (GOSAT) [14], SCanning Imaging Absorption spectroMeter for Atmospheric CHartographY (SCIAMACHY) [15], and Carbon Dioxide Observation Satellite Mission (TanSat) [16] boast advanced and custom-made optics and detectors. This design approach resulted in ultra-high spectral resolutions of 0.08–0.16 nm from space-based platforms, however, it also came with a significant budget allocation.

On the other hand, compact instruments on Nano-satellites such as the Argus 1000 micro-spectrometer onboard the second Canadian Advanced Nanospace eXperiment satellite (CanX-2) [17] incorporated miniaturisation concepts but had a lower spectral resolution of 5 nm compared to large space-based instruments. The Greenhouse Gases Satellite (GHGSat) is a NanoSat equipped with a passive spectrometer with a relatively high spectral resolution of 0.1 nm [18]. This spectrometer was specifically tuned to detect CH_4 concentrations within the narrow spectral channel of 1630-1675 nm.

In this paper, we present the development of RedEye-1, a small-sized, cost-effective instrument designed to provide valuable remote sensing capabilities. RedEye-1 was built using commercially available off-the-shelf components and operates within the spectral range of 1588–1673 nm, delivering a high spectral resolution of 0.5 nm. Notably, the development of RedEye-1 was successfully achieved at an estimated cost below $50k USD, with a significant portion of the budget allocated towards the InGaAs detector. This instrument enabled the simultaneous detection and quantification of CH_4 and CO_2 absorption bands and can serve as satellite validation for space-based instruments like the planned MethaneSAT [19] which covers the same spectral range as RedEye-1 and has similar spectral resolution.

2. Measurement strategy

The RedEye-1 instrument is a passive pushbroom imager that collects data in the flight direction. In addition to acquiring one-path radiance measurements from a ground-based platform, the instrument can also be directed towards Nadir from an airborne platform to capture the upwelling (reflected) solar radiance. The solar radiance profile collected contains crucial information regarding atmospheric constituents, which can then be processed and inferred through appropriate data reduction and analysis. From the Beer-Lambert law,

$$dI_\lambda = -I_\lambda K_\lambda \rho_l dl, \tag{1}$$

the intensity of light I_λ decreases as it travels through a medium with a path length dl and gas species number density ρ_l. The absorption dI_λ is directly proportional to dl and ρ_l, and the negative sign in the equation indicates the reduction in incident intensity I_λ due to the extinction function K_λ, which comprises both absorption and scattering cross sections.

Fig. 1 illustrates the pushbroom measurement configuration in which the imager on an uncrewed aerial vehicle (UAV) or aircraft platform is pointed directly below. This nadir viewing geometry ensures that the instrument has a clear line of sight to the Earth's surface, enabling the measurement of the reflected solar radiance with minimal atmospheric scattering.

OPTICS CONTINUUM

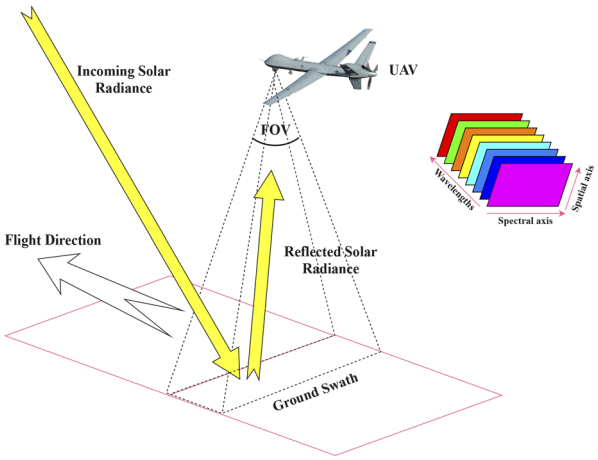

Fig. 1. The pushbroom hyperspectral imager uses a 2D focal plane array (FPA) to collect spectra of a swath. Motion in the along-track direction allows for a stacking of multiple images to form a hyperspectral datacube.

3. Instrument description

3.1. Optical design

We developed the optical design, shown in Fig. 2 (a) for the instrument, and (b) for the telescope, using the OpticStudio ZEMAX software, which enabled optical modelling and design. We improved the optical performance of our preliminary classical optical layout for the instrument, as described in [20], by modifying it to accommodate a new slit length which will be explored later in the slit subsection. Our optical design comprised of six main optical elements: the input slit, the collimating lens, the diffraction grating, the focusing/camera lens, a fold mirror, and the detector (camera/FPA). We opted for commercially available COTS components in an effort to minimise development costs. The specifications of RedEye-1 are summarised in Table 1.

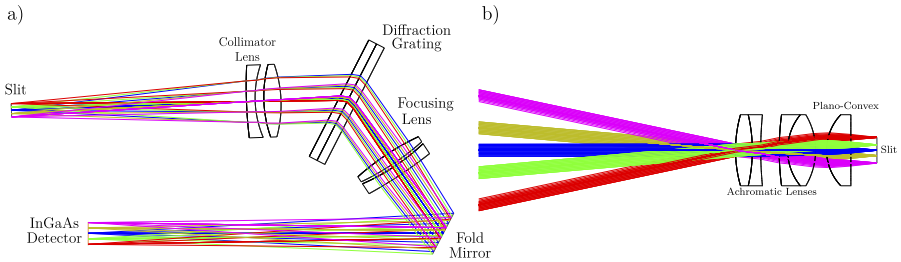

Fig. 2. a) Zemax model for the instrument optical layout, and b) telescope layout. The different colours indicate light at different wavelengths.

3.2. Telescope (fore-optics)

We used OpticStudio ZEMAX to evaluate a variety of optical designs before choosing the most suitable lenses. The primary consideration in the design of the telescope's optics was to effectively capture and focus the light rays originating from the field of view within the length of the slit. Our analysis revealed that the image produced by the commercially available 3 mm slit did not fully cover the spatial axis on the detector. As a result, we decided to use a custom 4.6 mm slit manufactured at the OptoFab node of the Australian National Fabrication Facility (ANFF).

OPTICS CONTINUUM

Table 1. RedEye-1 specifications.

Parameter	Value
Spectral Range	1588–1673 nm
Spectral Resolution	0.367 nm (calculated) and 0.365 nm (measured)
Spatial Resolution	0.125° (along-track)
Diffraction Grating	600 l/mm (VPH Transmission Grating)
Pixel pitch	15 µm
Detector	InGaAs-based, 640 (W) × 512 (L) pixels
Slit	25 µm (W) × 4.6 mm (L)
Field of View (FOV)	23°
Smile	3.5 pixels
Keystone	0.46 µm

Initially, we evaluated several optical designs in Zemax, including a Cooke-triplet layout. Although a Cooke-triplet offered a broad field of view (FOV), our slit length was only capable of fully accommodating light rays from a FOV of 23°. Therefore, we experimented with a new design consisting of two achromatic lenses and one plano-convex lens, all of which have a diameter of 12.7 mm.

The lenses were chosen from the ThorLabs catalogue and included anti-reflection coatings for the SWIR range (1050–1700 nm) applied to both surfaces.

3.3. Slit

As discussed in subsection 3.2, we used a custom 4.6 mm × 25 µm slit. The slit length l_{slit} and width w_{slit} played a crucial role in determining the telescope focal length through the relation:

$$f_{tel} = \frac{57.3}{\text{FOV}} \times l_{slit}, \tag{2}$$

where FOV is known to be 23° from the previous subsection 3.2, and f_{tel} is the effective focal length of the telescope which was 11.4 mm. The RedEye-1 instantaneous field of view (iFOV) defined its spatial resolution and this is calculated as

$$\text{iFOV} = 2\tan^{-1}\left(\frac{w_{slit}}{2f_{tel}}\right) \tag{3}$$

implying that it was 0.125° and 15° in the along-track and cross-track directions respectively. When deployed at an altitude of 3 km above sea level, the RedEye-1 ground sampling distance (GSD), a spatial resolution metric, was calculated to be 3.9 m following

$$\text{GSD} = \frac{P_{size}\,H}{f_{tel}}, \tag{4}$$

where P_{size} is the pixel pitch on the detector and H is the altitude [21]. However, due to the magnification of the slit on the detector, the GSD was reduced to approximately 2.37 m. Flying at an altitude of 3 km, RedEye-1 swath width of 1.21 km covers approximately 510 spatial pixels.

3.4. Collimator and camera optics

In order to collimate the light that passes through a 25 µm slit and achieve a spectral resolution (step) of 0.5 nm, the minimum focal length for the collimator is given by

$$f_{coli} = \frac{W_{slit}}{G_{disp} \times R_{spectral}} \tag{5}$$

OPTICS CONTINUUM

where W_{slit} represents the width of the slit, G_{disp} is the grating dispersion, and $R_{spectral}$ represents the desired spectral resolution (step). The minimum required focal length for the collimator, using the above equation, was approximately 80 mm.

After reviewing various optical component catalogues from manufacturers such as ThorLabs, Edmund Optics, Newport, we selected a pair of lenses that performed well in our optical design. These lenses formed an air-spaced achromatic lens system. The first lens was a negative fused silica meniscus with a focal length of -100 mm, and the second lens was a vacuum-grade bi-convex calcium fluoride (CaF_2) lens with a focal length of 50 mm. The combined focal length of these lenses was approximately 89.7 mm, and we found that the slit image was focused when placed at a distance of 89.7 mm from the collimator, provided the lenses were separated by a 4-mm precision spacer.

We evaluated another pair of lenses from the same collimator lens family, but with different focal lengths, in order to focus the diffracted light onto the image plane. We selected another vacuum-grade CaF_2 bi-convex lens and fused silica negative meniscus lens with -300 mm and 100 mm focal lengths respectively, giving a combined focal length of about 149 mm which was capable of achieving approximately 2.6 pixels per full width at half maximum (FWHM).

Both the collimator and camera lenses had a diameter of 25.4 mm and >90% clear aperture. The transmission rate of the Fused Silica and Calcium Fluoride lenses was over 93% and 95% in the SWIR spectral range respectively.

3.5. Diffraction grating and detector

We simulated and tested two off-the-shelf diffraction gratings with diameters 1" and 2" respectively, manufactured by Wasatch Photonics. Our spectral range and the selected Littrow angle of 29.2° dictated that we opt for the 2" (50.8 mm, with 45 mm clear aperture) volume phase holographic (VPH) grating. This grating had a spatial frequency of 600 lines/mm and a diffraction efficiency of over 80% in the relevant spectral range of RedEye-1.

To capture and record images with good quantum efficiency (QE) in the SWIR range, we selected an InGaAs-based detector (C-RED-3) manufactured by First Light Imaging with an array of 640 × 512 pixels and a pixel pitch of 15 µm. The detector had a volume of 55 mm (L) × 55 mm (W) × 60 mm (H), a mass of 0.230 kg, and a typical power consumption of 6.5 W. Figure 3 shows (a) the C-RED-3 unit and (b) its original equipment manufacturer (OEM) module. It can be controlled over a USB 3.0 with a maximum speed of 602 frames per second (FPS) and $< 40\ e^-$ readout noise.

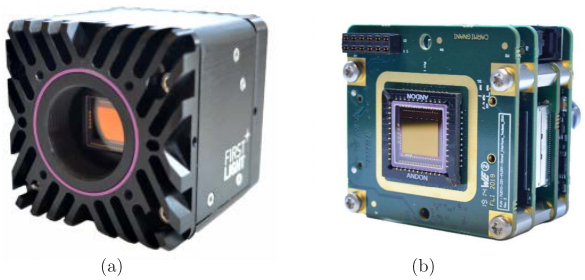

Fig. 3. (a) C-RED-3 unit and (b) its OEM module. (Credit: First Light Imaging)

3.6. Signal-to-noise ratio (SNR)

The Signal-to-noise ratio (SNR) is one of the most important features that sets the detection limit for any remote sensing instrument. To achieve the desired signal-to-noise ratio (SNR), a trade-off

OPTICS CONTINUUM

must be made between the SNR, the spatial resolution, and the spectral resolution which controls the number of photons (signal) entering the system. Generally, the required SNR for airborne hyperspectral imagers is in the order of hundreds [22]. For a global observation with an accuracy of 1% for CO_2 and 0.6-2% for CH_4 [23] from space, it was required to be 300:1 for the Japanese space-based GOSAT's imager (TANSO-FTS) [24]. Sensitivity analysis [25] showed that a 280:1 SNR to detect a 1% CO_2 change in the whole atmospheric column, from space, is achievable at a 0.12 nm spectral resolution.

Assuming that the SNR is limited by the photon shot noise, which is the square root of the mean signal value $\sigma_p = \sqrt{S_{mean}}$ for a Poisson distribution, it can be calculated as

$$\mathrm{SNR} \approx \frac{S}{\sigma_p} = \sqrt{S}\,, \tag{6}$$

where S is signal collected by a pixel on the detector and is influenced by the quantum efficiency η_Q of the detector, the number of the photons received per second, and the integration time.

The number of photons N_p is given by

$$\mathrm{N_p} = \frac{L\,\pi\,\tau}{4\,F/\#^2}\,\Delta\lambda\,A_{pixel}\,\Delta t\,\eta_Q\,\eta_G\frac{\lambda_c}{hc}\,, \tag{7}$$

where L is the radiance as a function of wavelength, τ is the optical transmission, $F/\#$ is the operating F-number of the optical system, $d\lambda$ is the spectral step, λ_c is the central wavelength, A_{pixel} is the pixel area, and η_G is the diffraction grating efficiency.

To estimate the SNR of RedEye-1, we used NASA's radiative transfer code (Planetary Spectrum Generator) to simulate the RedEye-1 spectrum with an albedo of 0.3, solar zenith angle of 30°, and altitude of 2000 m above sea level. This simulation provided the photon count for each wavelength. Subsequently, we employed the OpenHSI software library to estimate the SNR values at an exposure of 25 ms across the spectral range of RedEye-1. The estimated SNR values are shown in Figure 4. In the majority of RedEye-1's spectral range, the quantum efficiency (QE) exceeded 70%, with the exception of wavelengths ranging from 1660–1673 nm, where it remained above 65% (manufacturer supplied data). While higher QE improves the SNR, it can also be improved through temporal or spatial averaging, although, such averaging methods can impact the spatial resolution [26].

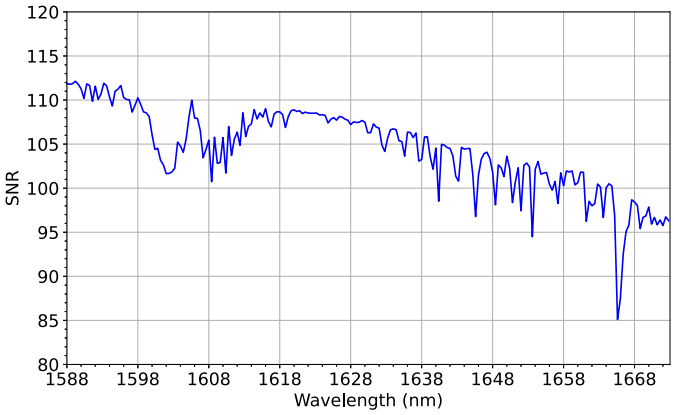

Fig. 4. Estimated SNR across RedEye-1's spectral range.

OPTICS CONTINUUM

3.7. SolidWorks CAD model, manufacturing and assembly

Despite the feasibility of 3D-printing the housing components for RedEye-1, we chose to utilize CNC manufacturing at the School of Physics design and prototyping facility. We designed a preliminary SolidWorks CAD model, shown in Fig. 5(a), that incorporated two joints. These joints served to securely house and protect both the grating, shown in 5(b) and fold mirror (located within joint 2 in Figure 5(a)), as well as two mounting plates that provided support for the lens tubes. Figure 5(c) shows a top-view of the complete assembly of RedEye-1 sitting on a motion control plate. To minimise the weight of the instrument, we incorporated holes into the mounting plates and added precision chamfers on the joints edges. These design features effectively reduced the mass while maintaining structural integrity.

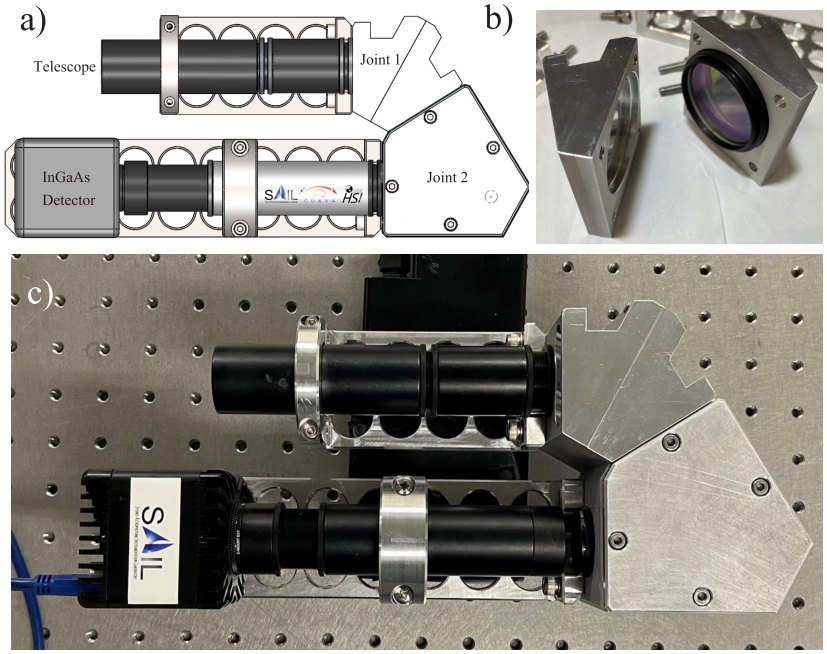

Fig. 5. (a) RedEye-1 CAD model. (b) Joint 1 hosting the grating. (c) Top-view of RedEye-1 after assembly.

The diffraction grating is a crucial component that requires careful protection against vibrations, cracking, and any movement along its axis. To address these concerns, we implemented several measures in the design process. Firstly, The grating, housed in a 2.2" (55.9 mm) lens tube with a 12.7 mm thread depth (SM1), was securely locked in place with a retaining ring. Secondly, the lens tube containing the grating was placed inside the CNC-machined joint 1, as shown in Figure 5(b). This joint was attached and locked in place with four M6 screws, providing added protection to the grating and ensuring a perfect seal to minimise stray light. Finally, the second joint held the fold mirror, which was responsible for directing the diffracted beam towards the detector. These design steps ensured that the diffraction grating was protected and securely held in place, allowing for accurate and reliable measurements.

The mounting plates were attached and fixed to the sides of the joints. The first plate was positioned under the SM1 lens tube that housed the telescope, filter, and collimator, while the second plate was located beneath another SM1 lens tube that encased the focusing lens. The second plate was securely attached to the bottom of the detector. For added rigidity and stability, both SM1 lens tubes were secured in place with two half-ring clamps. This ensured that the tubes

OPTICS CONTINUUM

remained securely in place even during any movements or vibrations, ensuring the stability and accuracy of the instrument's measurements.

4. Calibration

4.1. Wavelength calibration

Accurate wavelength calibration is essential for obtaining reliable measurements in spectrometry. The established method for wavelength calibration typically involves determining the centres of emission peaks on the detector and counting the number of peaks within the instrument's spectral range [27–29]. To perform the wavelength calibration, we used three laser sources: a tunable laser that emitted lines in the spectral range 1520–1600 nm, and two additional laser sources that emitted lines at 1608.76 nm and 1653.72 nm, respectively. The third laser source emitted a wavelength corresponding to one of the CH_4 absorption lines in the SWIR range. To guarantee the accuracy of the laser source outputs, we connected each source to a Michelson interferometer-based wavemeter. This allowed us to verify that the wavelengths were accurate to approximately 3×10^{-4} nm.

To control the instrument and collect spectral lines from the three laser sources, we used the OpenHSI Python library [7].

We employed a peak detection algorithm to associate each pixel on the detector with its corresponding wavelength. This was done by finding the peak for each laser line, as shown in the top panel of Fig. 6.

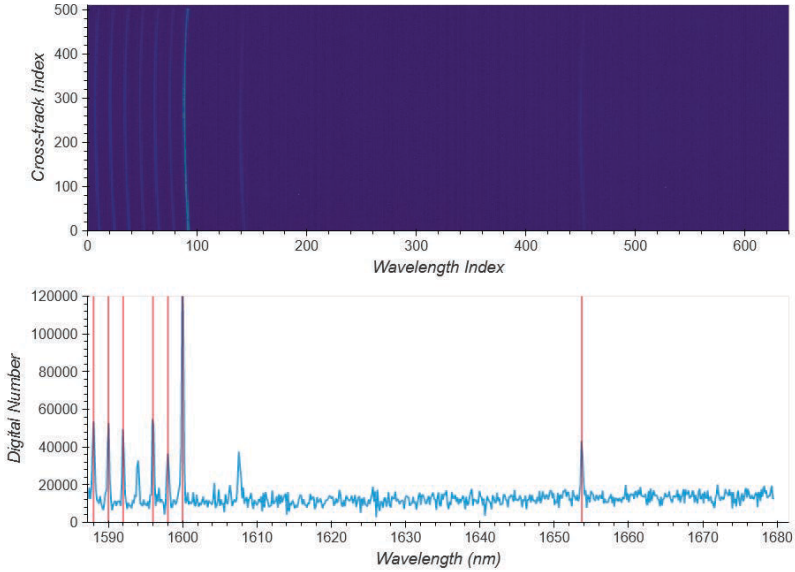

Fig. 6. SWIR image of the selected laser lines from three different laser sources (top panel). The curve fits to peaks in the spectra of the laser lines have vertical red lines showing the peaks selected for the fit (bottom panel)

To refine the center wavelengths, we applied a curve fit to each peak, assuming a Gaussian shape, as shown in the bottom panel of Fig. 6. The vertical red lines in the bottom panel represent the peaks we obtained from the laser sources and then used to perform the calibration fit. The relationship between wavelength and pixel position on the detector is known to be a third-order polynomial [30]. Figure 7 illustrates the pixel numbers corresponding to the predicted wavelengths with a cubic fit (top panel) and the residuals (bottom panel). It is important to note

OPTICS CONTINUUM

that while efforts were made to find additional emission lines within RedEye-1 narrow spectral range, they were either too weak to be detected or simply did not exist.

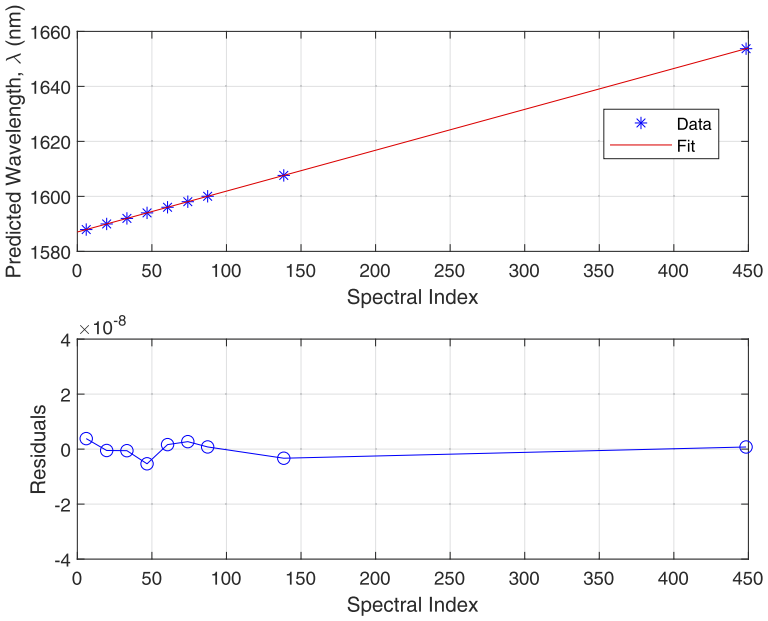

Fig. 7. Curve fit to the wavelength as a function of the observed pixel location on the detector using laser calibration peaks (top panel) and their residuals (bottom panel).

4.2. Radiometric calibration

The basic form of data that the detector outputs on its y-axis is digital numbers (DN) or counts. These counts must be converted to spectral radiance units $\mu W/cm^2/sr/nm$ for physically useful and meaningful measurements. We mounted the instrument on a lab scissor jack and pointed its telescope (fore-optics) directly to an integrating sphere's aperture to perform the radiometric calibration at full illumination. We collected the raw counts for various integration times while covering the aperture in a dark room to account for the detector dark current and labelled them as C_{dark}. The raw counts (with dark current subtracted) when the integrating sphere was set to different luminance values are labelled as reference counts C_{ref}. The dark current counts C_{dark} are subtracted from the raw counts C acquired and divided by the reference counts at a given luminance C_{ref}. The resulting dimensionless ratio is then multiplied by the corresponding luminance value L_{ref} to obtain units of luminance. The manufacturer provides the spectral radiance $L_{\lambda,mnf}$ at a given luminance of 53,880 Cd/m^2 so by scaling to this curve (Fig. 8) we were able to convert counts to spectral radiance L_λ. This is summarised in equation form as

$$L_\lambda = \left(\frac{C - C_{dark}}{C_{ref}} \times L_{ref}\right) \times \left(\frac{L_{\lambda,mnf}}{53,880}\right). \tag{8}$$

For our calibration file, we used luminances from 0–10,000 Cd/m^2 in steps of 1,000 Cd/m^2, then included 15,000 and 20,000 Cd/m^2. This range covered the expected luminance indoors and outdoors when we pointed the sensor to a Spectralon panel on a sunny day. At high exposures and high luminances, the detector saturated so those data points were discarded. For each value, we averaged 100 frames to reduce random noise.

OPTICS CONTINUUM

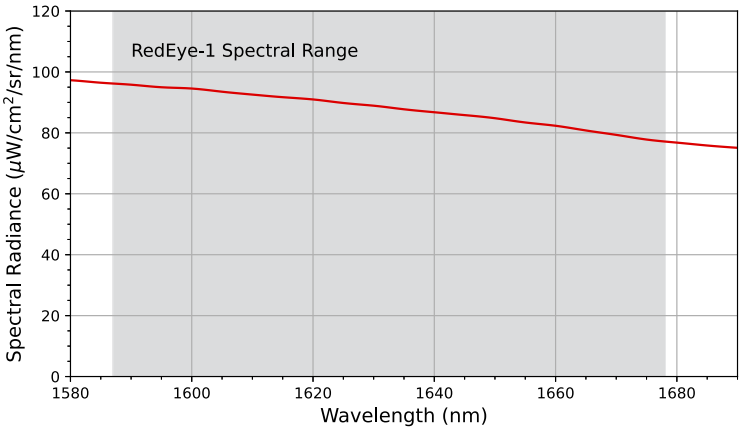

Fig. 8. At-aperture spectral radiance reference collected at 53,880 Cd/m^2 luminance. The shaded area indicates the spectral range for RedEye-1.

5. Performance

5.1. OpticStudio ZEMAX simulation

We used OpticStudio ZEMAX to evaluate the optical performance of RedEye-1. We generated a spot diagram (Fig. 9) to represent selected points on the positive x-axis of the slit. The spot diagram illustrates the ray spots originating from three different positions: the centre of the slit, a position 1.15 mm away from the slit centre, and the farthest positive edge of the slit, which was 2.3 mm away from the slit centre. The wavelength range corresponded to RedEye-1's spectral range centred at 1630.5 nm. At the image plane, the spots exhibited a generally consistent performance across the wavelengths, with the exception of the extreme edges which deviated from the uniform pattern. The black circle represents the Airy disk, which had a diameter of 16.33 μm and represents the diffraction limit of the system.

5.2. Spectral resolution

The slit width, pixel size (P_{size}), and spectral range ($\Delta\lambda$) played critical roles in forming the instrument spectral resolution, FWHM, which can be calculated theoretically as

$$\text{FWHM} = \frac{W_{slit} \times \text{RF} \times \Delta\lambda}{\#\text{pixels} \times P_{size}}, \tag{9}$$

where RF denotes the resolution factor 1.66, defined by the relationship between the slit width and the pixel size, and #pixels specifies the number of spectral pixels. This yielded a theoretical FWHM of approximately 0.367 nm occupying $\approx$ 2.6 pixels, which aligned closely with the measured FWHM, as demonstrated in the following laboratory evaluation.

We evaluated the spectral resolution of RedEye-1 by computing the point spread functions (PSFs) of two neighbouring wavelengths. Fig. 10(a) shows the Huygens PSFs for wavelengths 1630.5 nm and 1631 nm separated by 0.5 nm, the intended spectral resolution for RedEye-1. The normalised intensity peaks of the two adjacent wavelengths showed that the system can achieve a spectral resolution better than 0.5 nm.

To practically test the spectral resolution, we used a SWIR tunable laser source and generated two adjacent wavelengths separated by a 0.5 nm and plotted their profiles. Figure 10(b) shows wavelengths profiles of 1590.00 nm (blue asterisk) and 1590.5 nm (red asterisk) separated by a 0.5 nm. They are Gaussian fitted (dashed lines) and summed together (black line). The measured FWHM in Fig. 10(b) is approximately 0.365 nm, closely matching the calculated FWHM.

OPTICS CONTINUUM

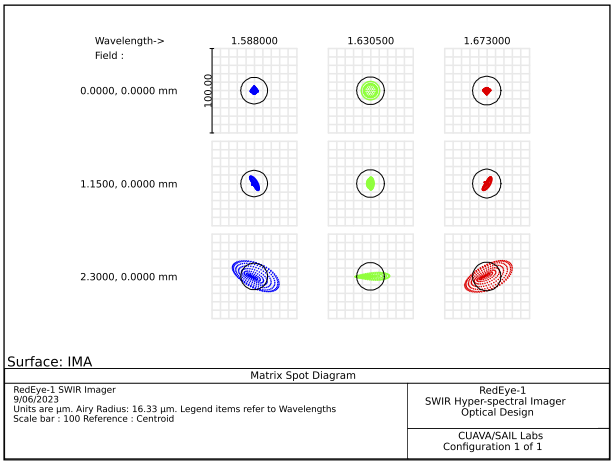

Fig. 9. Spot diagram for selected points on the positive x-axis of the slit for the first, central, and last wavelengths. The first row shows spots that corresponded to the rays originating from centre of the slit. The second raw row represents rays spots at a 1.15 mm distance from the slit centre. The third row shows spots originating from the extreme positive edge of the slit, 2.3 mm away from the slit centre, and arriving at the edge of the detector. The columns show the RedEye-1's spectral coverage centred at 1630.5 nm.

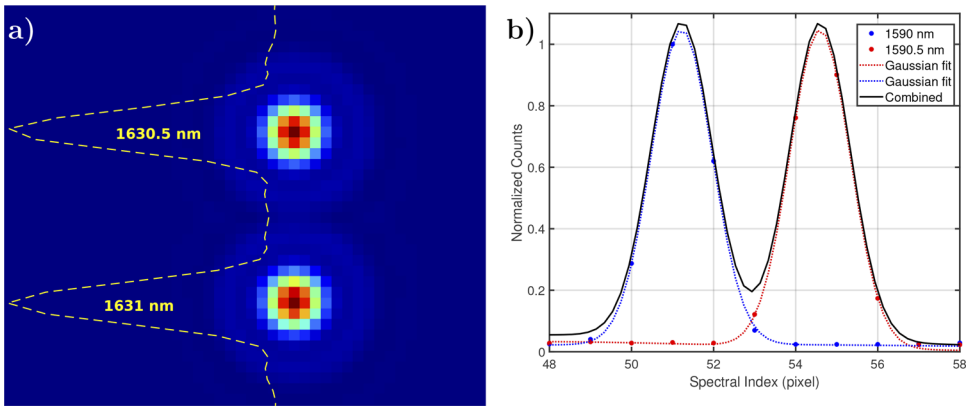

Fig. 10. (a) Huygens point spread function (PSF) of RedEye-1's central wavelength of 1630.5 nm and an adjacent wavelength of 1631 nm with a spectral step of 0.5 nm, along with their corresponding normalised radiance intensity profiles.(b)Tunable laser profiles for wavelengths 1590.00 nm (blue asterisk) and 1590.5 nm (red asterisk). The dashed lines are the Gaussian fit for the wavelengths profiles and black line is their sum.

OPTICS CONTINUUM

According to the Rayleigh criterion [31], two intensity profiles are just resolved when the peak of the first profile lies directly over the minimum of the second adjacent profile. However, this criterion becomes difficult to use when profiles do not have zero values at their minima. This leads to the generalised form of Rayleigh criterion (Robertson-Rayleigh) which states that the local minimum of the sum of the two peaks should be at most 81% [32] of their intensity value. In Fig. 10(b), the two peaks showed a local minimum that is below 81% of their intensity value when they are summed together.

5.3. Smile and keystone

Smile is a spectral distortion (misregistration) that is a property of the instrument slit height [33] and causes a wavelength shift. The keystone is a spatial misregistration that causes a shift in the spatial pixels and is a function of wavelength [34]. They are optical distortions that are always present in pushbroom hyperspectral instruments and must be characterised and corrected. Zemax simulation indicated that the RedEye-1 smile, shown in Fig. 11(a) was approximately 3.5 pixels at the edges of the slit for selected wavelengths across the RedEye-1 spectral range. Moreover, Keystone effect, shown in Fig. 11(b), was minimal in the system where the longest wavelength (1673 nm), had only 0.48 um keystone difference compared to the shortest wavelength (1588 nm). By employing the 15 mu pixel pitch InGaAs detector, the 0.48 um keystone effect will not be noticeable. While smile and keystone can be corrected either during the optical design phase [35] or in the post processing stage [36–38], the OpenHSI processing pipeline performs smile correction during the collection of raw datacubes.

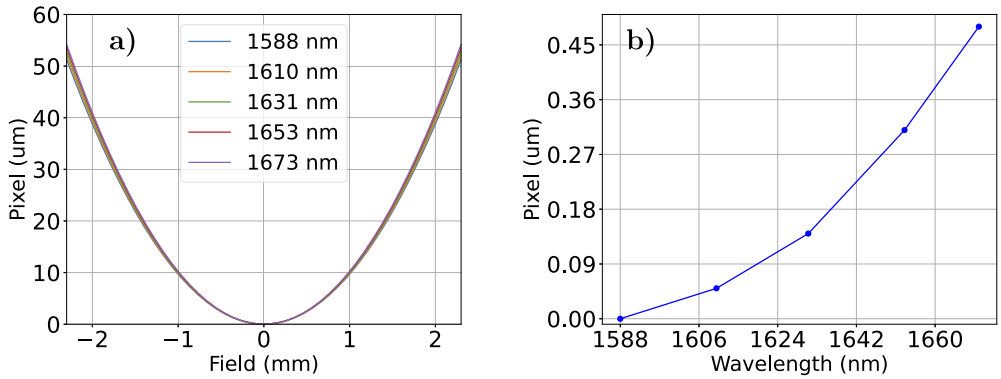

Fig. 11. Smile (a) and keystone (b) effect for RedEye-1.

5.4. Hyperspectral datacube image

We set up the RedEye-1 on a motion control plate and aimed it towards the north side from the physics building to scan across a scene. The target scene consisted of trees, buildings, and a significant portion of the sky. Using RedEye-1, we collected and produced a SWIR datacube image of the scene, as shown in Fig. 12. The RedEye-1 system scanned from left to right and acquired 1200 lines with a 65 ms exposure time.

We carried out initial data reduction and analysis on the datacube image obtained from the RedEye-1's first acquisition. We started by eliminating the dark current from the image, then examined each pixel's spectrum along the slit line. Fig. 13 (a) shows selected lines of the spatial pixels featuring the absorption bands/lines of CO_2 and CH_4 in the shadowed areas. We also computed the average of the spectral profiles along the slit spatial axis and produced an atmospheric profile, as depicted in Fig. 13 (b). The atmospheric profile shows the CO_2 and CH_4

OPTICS CONTINUUM

Fig. 12. RedEye-1 SWIR image at 1600 nm captured from the north side of the Physics building, University of Sydney.

absorption lines within RedEye-1's spectral coverage, providing a single-pass measurement of scattered photons from the clouds.

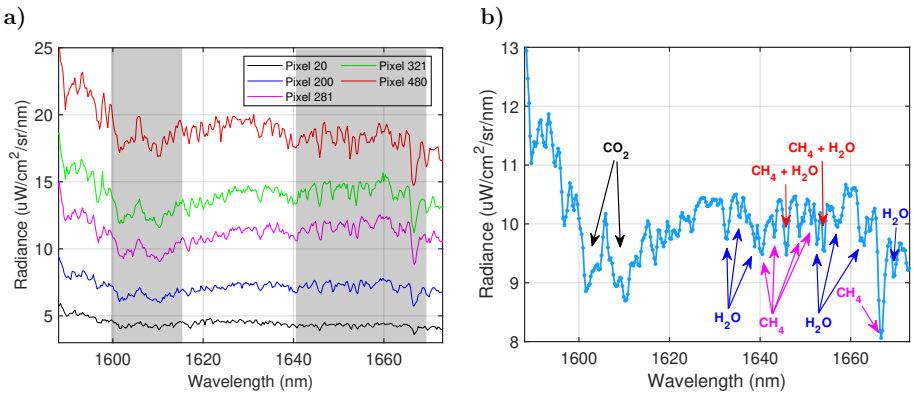

Fig. 13. a) Spectral lines from selected pixels along the slit line. b) The averaged spectral profile of the slit lines across the spectral range of RedEye-1. Arrows indicate absorption lines/bands for CO_2 (black), H_2O (blue), CH_4 (pink), and interference between CH_4 and H_2O lines (red).

It is worth noting that the retrieval of CH_4 and CO_2 concentrations from the atmospheric profile goes beyond the scope of this paper and will be addressed once the airborne reconnaissance is completed. As previously outlined in the measurement strategy section, the ultimate goal of RedEye-1 is to conduct airborne reconnaissance over various locations and retrieve the concentration of atmospheric constituents. In this scenario, solar radiance will pass through the atmospheric layer twice before it is intercepted by RedEye-1, which will be deployed at an altitude, enabling a two-path measurement of the solar radiance.

6. Future work

RedEye-1 will undergo UAV flights to assess its low-cost design under uncontrolled environmental conditions. In collaboration with the UAV team in the ARC Training centre for CubeSats, UAVs, and Their Applications (CUAVA), it will embark on its first atmospheric reconnaissance mission.

OPTICS CONTINUUM

Additionally, we have plans to re-evaluate and optimise the system specifically for space-based measurements from a CubeSat platform in the near future.

7. Conclusion

We reported on and described our first prototype of a small SWIR hyperspectral imager that operates in the spectral range from 1588 nm to 1673 nm with a spectral resolution of 0.5 nm. We built and developed the imager using commercial off-the-shelf components to reduce the development cost, with the InGaAs-based detector driving the budget allocation. We added mounting plates and two joints, which hosted the diffraction grating and fold mirror preceding the imager. Although these parts could be 3D-printed, we chose to use CNC machining service at the design and prototyping facility in the School of Physics. We calibrated RedEye-1 spectrally and radiometrically, collected and analysed the first ground-based datacube image, and showed a one-path, ground-based observation of RedEye-1's spectral profile featuring absorption lines of CO_2 and CH_4. We successfully demonstrated the ability of RedEye-1 to achieve the intended spectral resolution while producing high-quality images. This establishes its suitability for airborne platforms and ground-based validation of space-based data.

Funding. Australian Research Council Industrial Transformation Training Centre for CubeSats, UAVs, and Their Applications (CUAVA); Sydney Astrophotonic Instrumentation Laboratory (SAIL) University of Sydney; Saudi Arabian Cultural Mission.

Acknowledgment. The authors acknowledge the role of the senior technical officers at the design and prototyping facility, School of Physics, University of Sydney, in manufacturing the instruments parts. Mr. Caleb Moya Gudu, and Mr. Nagaraja Panduranga provided technical guidance over the CAD design to make it manufacturable and conducted high-precision CNC machining work. This work was performed in part at the OptoFab node of the Australian National Fabrication Facility (ANFF) with Commonwealth and NSW State Government funding.

Disclosures. The authors declare no conflicts of interest.

Data availability. Data underlying the results presented in this paper are not publicly available at this time but may be obtained from the authors upon reasonable request.

References

1. M. De Biasio, T. Arnold, R. Leitner, *et al.*, "Uav-based environmental monitoring using multi-spectral imaging," Proc. SPIE **7668**, 766811 (2010).
2. V. Lebourgeois, A. Bégué, S. Labbé, *et al.*, "A light-weight multi-spectral aerial imaging system for nitrogen crop monitoring," Precision Agriculture **13**, 525–541 (2012).
3. M. T. Eismann, A. D. Stocker, and N. M. Nasrabadi, "Automated hyperspectral cueing for civilian search and rescue," Proceedings of the IEEE **97**, 1031–1055 (2009).
4. X. Briottet, Y. Boucher, A. Dimmeler, *et al.*, "Military applications of hyperspectral imagery," Proc. SPIE **6239**, 62390B (2006).
5. F. Sigernes, M. Syrjäsuo, R. Storvold, *et al.*, "Do it yourself hyperspectral imager for handheld to airborne operations," Optics express **26**, 6021–6035 (2018).
6. M. B. Henriksen, E. F. Prentice, C. M. van Hazendonk, *et al.*, "Do-it-yourself vis/nir pushbroom hyperspectral imager with c-mount optics," Optics Continuum **1**, 427–441 (2022).
7. Y. Mao, C. H. Betters, B. Evans, *et al.*, "OpenHSI: A complete open-source hyperspectral imaging solution for everyone," Remote Sensing **14**, 2244 (2022).
8. P. Jain, "Greenhouse effect and climate change: scientific basis and overview," Renewable Energy **3**, 403–420 (1993).
9. V. Ramanathan and Y. Feng, "Air pollution, greenhouse gases and climate change: Global and regional perspectives," Atmospheric environment **43**, 37–50 (2009).
10. T. R. Anderson, E. Hawkins, and P. D. Jones, "Co2, the greenhouse effect and global warming: from the pioneering work of arrhenius and callendar to today's earth system models," Endeavour **40**, 178–187 (2016).
11. R. E. Dickinson and R. J. Cicerone, "Future global warming from atmospheric trace gases," Nature **319**, 109–115 (1986).
12. D. A. Lashof and D. R. Ahuja, "Relative contributions of greenhouse gas emissions to global warming," Nature **344**, 529–531 (1990).
13. A. Eldering, C. W. O'Dell, P. O. Wennberg, *et al.*, "The orbiting carbon observatory-2: First 18 months of science data products," Atmospheric Measurement Techniques **10**, 549–563 (2017).
14. T. Hamazaki, Y. Kaneko, A. Kuze, *et al.*, "Fourier transform spectrometer for greenhouse gases observing satellite (gosat)," Proc. SPIE **5659**, 73–80 (2005).

OPTICS CONTINUUM

15. H. Bovensmann, M. Buchwitz, J. Frerick, *et al.*, "Sciamachy on envisat: In-flight optical performance and first results," Proc. SPIE **5235**, 160–173 (2004).
16. Y. Bi, Z. Yang, S. Gu, *et al.*, "Impacts of aerosol and albedo on tansat co2 retrieval using the near infrared co2 bands," Proc. SPIE **9259**, 925915 (2014).
17. N. Alsalem, C. Tsouvaltsidis, C. Roberts, *et al.*, "Clouds effect on the atmospheric total column carbon dioxide retrieval by space orbiting argus 1000 micro-spectrometer: introductory study," Proc. SPIE **10776**, 107760Z (2018).
18. D. J. Varon, D. J. Jacob, J. McKeever, *et al.*, "Quantifying methane point sources from fine-scale satellite observations of atmospheric methane plumes," Atmospheric Measurement Techniques **11**, 5673–5686 (2018).
19. R. R. Rohrschneider, S. Wofsy, J. E. Franklin, *et al.*, "The methanesat mission," *35th Annual Small Satellite Conference* (2021).
20. N. Alsalem, C. Betters, S. Leon-Saval, *et al.*, "Cuava ingaas-based, short wavelength infrared (swir) instrument for atmospheric reconnaissance: preliminary design," Proc. SPIE **11852**, 118526A (2021).
21. Á. Q. Valenzuela and J. C. G. Reyes, "Basic spatial resolution metrics for satellite imagers," IEEE Sensors J. **19**(13), 4914–4922 (2019).
22. Y. Chen, Y. Ji, J. Zhou, *et al.*, "Computation of signal-to-noise ratio of airborne hyperspectral imaging spectrometer," in *2012 International Conference on Systems and Informatics (ICSAI2012)*, (IEEE, 2012), pp. 1046–1049.
23. J. Yoshida, T. Kawashima, J. Ishida, *et al.*, "Prelaunch performance test results of tanso-fts and cai on gosat," Proc. SPIE **7082**, 708214 (2008).
24. A. Kuze, H. Suto, K. Shiomi, *et al.*, "On-orbit performance and level 1 data processing of tanso-fts and cai on gosat," Proc. SPIE **7474**, 74740I (2009).
25. Q. Wang, Z.-D. Yang, and Y.-M. Bi, "Spectral parameters and signal-to-noise ratio requirement for tansat hyper spectral remote sensor of atmospheric co2," Proc. SPIE **9259**, 92591T (2014).
26. N. Z. M. Alsalem, "*Sensitivity studies for argus 1000 micro-spectrometer: Measurements of atmospheric total column carbon dioxide by reflected sunlight*," (York University Library, Toronto, Canada, 2016).
27. Y. Sun, C. Huang, G. Xia, *et al.*, "Accurate wavelength calibration method for compact ccd spectrometer," JOSA A **34**, 498–505 (2017).
28. A. K. Gaigalas, L. Wang, H.-J. He, *et al.*, "Procedures for wavelength calibration and spectral response correction of ccd array spectrometers," Journal of research of the National Institute of Standards and Technology **114**, 215 (2009).
29. A. Labiano, I. Argyriou, J. Álvarez-Márquez, *et al.*, "Wavelength calibration and resolving power of the jwst miri medium resolution spectrometer," Astronomy & Astrophysics **656**, A57 (2021).
30. G. Polder, G. W. van der Heijden, L. P. Keizer, *et al.*, "Calibration and characterisation of imaging spectrographs," Journal of Near Infrared Spectroscopy **11**, 193–210 (2003).
31. L. Rayleigh, "Xxxi. investigations in optics, with special reference to the spectroscope," The London, Edinburgh, and Dublin Philosophical Magazine and Journal of Science **8**, 261–274 (1879).
32. J. G. Robertson, "Quantifying resolving power in astronomical spectra," Publ. Astron. Soc. Aust. **30**, e048 (2013).
33. M. B. Henriksen, J. L. Garrett, E. F. Prentice, *et al.*, "Real-time corrections for a low-cost hyperspectral instrument," in *2019 10th Workshop on Hyperspectral Imaging and Signal Processing: Evolution in Remote Sensing (WHISPERS)*, (IEEE, 2019), pp. 1–5.
34. M. B. Henriksen, E. F. Prentice, T. A. Johansen, *et al.*, "Pre-launch calibration of the hypso-1 cubesat hyperspectral imager," in *2022 IEEE Aerospace Conference (AERO)*, (IEEE, 2022), pp. 1–9.
35. P. Mouroulis, R. O. Green, and T. G. Chrien, "Design of pushbroom imaging spectrometers for optimum recovery of spectroscopic and spatial information," Applied Optics **39**, 2210–2220 (2000).
36. A. Fridman, G. Høye, and T. Løke, "Resampling in hyperspectral cameras as an alternative to correcting keystone in hardware, with focus on benefits for optical design and data quality," Optical Engineering **53**, 053107 (2014).
37. K. A. Riihiaho, M. A. Eskelinen, and I. Pölönen, "A do-it-yourself hyperspectral imager brought to practice with open-source python," Sensors **21**, 1072 (2021).
38. K. C. Lawrence, B. Park, W. R. Windham, *et al.*, "Calibration of a pushbroom hyperspectral imaging system for agricultural inspection," Trans. ASAE **46**, 513 (2003).